


Article

Optical Trapping and Manipulation of Nanoparticles on Plasmonic Silicon-Nanostructured Array Coating on Silicon Film

Wei Zhou ^{1,*}, Debao Wang ¹, Yanru Ren ¹, Jingwei Lv ¹, Ying Yu ¹, Wei Li ¹, Xinchen Xu ¹, Paul K. Chu ^{2,3,4} 
and Chao Liu ¹

¹ School of Physics and Electronic Engineering, Northeast Petroleum University, Daqing 163318, China; w20201226@yeah.net (D.W.); r17860231652@163.com (Y.R.); lvjingwei2009123@126.com (J.L.); yy1724983951@163.com (Y.Y.); liiw1859@163.com (W.L.); xuxinchen2023@163.com (X.X.); msm-liu@126.com (C.L.)

² Department of Physics, City University of Hong Kong, Hong Kong 999077, China; paul.chu@cityu.edu.hk

³ Department of Materials Science and Engineering, City University of Hong Kong, Hong Kong 999077, China

⁴ Department of Biomedical Engineering, City University of Hong Kong, Hong Kong 999077, China

* Correspondence: zhouwei1980@nepu.edu.cn

Abstract: A silicon-nanostructured array coating on silicon film (SAS film) is designed based on the plasmonic optical tweezer and demonstrated for optical trapping and manipulation of nanospheres with negligible impact on the local thermal conditions. The electric field enhancement, optical force, and trapping potential of the SAS film are investigated by the finite element method. The trapping position is affected by the incident light wavelength, structure of the nanoarray, and refractive index of the nanospheres. The presence of four energy wells around the nanoarray suggests that it is possible to trap multiple nanoparticles. Moreover, the circularly polarized light, Gaussian beam, and silicon nanoarray facilitate the trapping of nanoparticles. This study showcases the potential of SAS film as optical tweezers to capture nanoparticles for the development of nanophotonic devices.

Keywords: optical tweezers; electric field enhancement; trapping potential; silicon-nanostructured array coatings on silicon film; circularly polarized light



Citation: Zhou, W.; Wang, D.; Ren, Y.; Lv, J.; Yu, Y.; Li, W.; Xu, X.; Chu, P.K.; Liu, C. Optical Trapping and Manipulation of Nanoparticles on Plasmonic Silicon-Nanostructured Array Coating on Silicon Film. *Coatings* **2023**, *13*, 1388. <https://doi.org/10.3390/coatings13081388>

Academic Editor: Luca Tomassetti

Received: 3 July 2023

Revised: 31 July 2023

Accepted: 1 August 2023

Published: 7 August 2023



Copyright: © 2023 by the authors. Licensee MDPI, Basel, Switzerland. This article is an open access article distributed under the terms and conditions of the Creative Commons Attribution (CC BY) license (<https://creativecommons.org/licenses/by/4.0/>).

1. Introduction

The optical tweezer has emerged as an important device for the noninvasive manipulation of mesoscopic objects since the pioneering work of Ashkin [1] and has led to fascinating applications such as DNA stretching [2], photonic force microscopy [3], and DNA dynamics analysis [4]. The conventional method of optical tweezing involves the use of a tightly focused laser beam to produce a gradient force that can be utilized to manipulate particles [5]. However, traditional optical tweezers for high-precision particle manipulation typically require a high laser power which may irreversibly destroy heat-sensitive materials like DNA and proteins [6]. Moreover, the diffraction limit restricts light propagation in free space below the sub-wavelength range, making the trapping position uncertain. Recent developments in fabrication methods and nano-optics have spurred the development of plasmonic optical tweezers (POTs), where the plasmonic waves amplify the optical forces exerted by the device [7]. The current technique involves imposing a gradient force on the particles by the amplified electromagnetic field that arises from localized surface plasmon resonance (LSPR). Therefore, the amplification and localization of an electromagnetic field at a specific location, which is referred to as a plasmonic hotspot [8,9], result in a stronger trapping potential well that enhances the efficacy of nanoparticle trapping.

Metallic nanostructures have the characteristics of LSPR which stems from the collective electron oscillations on the surface of plasmonic nanoparticles. POTs primarily rely on the amplified and confined electromagnetic fields around nanostructures, such

as nanoapertures [10], tetramers [11], disk-ring pairs [12], and nanoholes [13]. Gao et al. have shown that the optical pulling force exerted on active plasmonic nanoparticles due to Fano resonance can be enhanced by two orders of magnitude compared to a single active nanoparticle [14] and Jiang et al. have used metal disks to generate resonance at specific wavelengths to control the trapping positions [15]. However, the strong POT consisting of plasmonic nanoparticles produced by LSPR is prone to thermal damage due to the relatively large absorption loss at the optical frequency [16]. Hence, all-dielectric nanostructures comprising silicon and germanium structures have been investigated as they offer appealing features such as low losses and high refractive indexes.

High-refractive-index dielectric nanostructures have attracted extensive attention and play a crucial role in enhancing the local fields. In addition, the optical resonance observed from all-Si nanoantennas has the potential to surpass the diffraction limit, thus enabling control of the incident light on the subwavelength scale [17]. Experimental evidence has demonstrated that all-Si nanoantennas indeed possess the capability of capturing individual particles, and their interactions with confined light fields have been examined [18–20]. Nevertheless, the investigation of optical manipulation utilizing all-dielectric nanoantennas is still in the early stage with regard to optical trapping and manipulation of nanostructures. Since these functionalities can be achieved by plasmonic techniques, there is a growing interest in all-dielectric nanostructures, especially from the perspective of precise manipulation.

Herein, optical trapping by a single dielectric nanosphere (NS) in a silicon-nanostructured array coating on silicon film is demonstrated upon illumination by polarized light. In contrast to resonances observed from individual plasmonic structures, the nanoparticle array exhibits higher resonance peaks due to the interactions between particles. The local field enhancement and optical force generated by the nanostructured array are investigated, including the dependence of the force on the height and width of the nanostructured array as well as the radius and refractive properties of the nanosphere. Nanoparticles can be captured by two traps simultaneously using circularly polarized illumination and a Gaussian beam. The results reveal that the nonperturbative all-Si tweezer can be generated by strong exciton–plasmon coupling. It has a large practical potential with respect to optical manipulation and optical assembly of strong-coupling systems on Si chips, boding well for life science and biological research as well as commercial applications.

2. Model and Method

2.1. Method of Multipole Decomposition

The process of light scattering can be understood as the re-emission of light as a consequence of the polarized charge current in the scattering medium [21]. In the context of classical electrodynamics, the distributions of the polarized charge current can be divided into three categories of dynamic multipoles: electric multipoles, magnetic multipoles, and toroidal multipoles [22]. The method of multipole decompositions, including electric dipole moment P_α (ED), magnetic dipole moment M_α (MD), toroidal dipole moment T_α (TD), electric quadrupole moment $Q_{\alpha\beta}^e$ (EQ), and magnetic quadrupole moment $Q_{\alpha\beta}^m$ (MQ), are typically utilized to analyze the scattering cross-section (SCS) and near-field characteristics of nanosystems. The general expressions are described as follows [21,23]:

$$P_\alpha = \frac{1}{i\omega} \int J_\alpha d^3r \quad (1)$$

$$M_\alpha = \frac{1}{2c} \int [r \times J]_\alpha d^3r \quad (2)$$

$$T_\alpha = \frac{1}{10c} \int [(r \times J)_{r_\alpha} - 2r^2 J_\alpha] d^3r \quad (3)$$

$$Q_{\alpha\beta}^e = -\frac{1}{i\omega} \int \left[r_\alpha J_\beta - \frac{2}{3} \delta_{\alpha\beta} (r \cdot J) \right] d^3r \tag{4}$$

$$Q_{\alpha\beta}^m = \frac{1}{3c} \int [[r \cdot J]_\alpha r_\beta + r_\alpha [r \times J]_\alpha] d^3r \tag{5}$$

where r, J , and the subscripts $\alpha, \beta = x, y, z$ denote the position vector, polarization current density excited in the antenna, and the components of EQ and MQ, respectively. The radiation power I comprising the aforementioned multipole moments can be calculated by Equation (6) [24]:

$$I = \frac{1}{8\pi\epsilon_0} \left[\frac{2\omega^4}{3c^3} |P|^2 + \frac{2\omega^4}{3c^3} |M|^2 + \frac{4\omega^5}{3c^4} \text{Im}(P * T) + \frac{2\omega^6}{3c^5} |T|^2 + \frac{\omega^6}{20c^5} \sum |T|^2 + \frac{\omega^6}{20c^5} \sum |Q^e|^2 + \frac{\omega^6}{20c^5} \sum |Q^m|^2 \right] \tag{6}$$

where ω, c , and ϵ_0 represent the angular frequency, speed of light, and vacuum dielectric constant, respectively. The scattering cross-section C_{sca} is described as follows [24]:

$$C_{sca} = \frac{I}{I_{inc}} \tag{7}$$

where I_{inc} is the radiation power of the incident light wave.

2.2. Maxwell Stress Tensor Method

The electromagnetic field exerts optical forces on the particle, namely the scattering force and gradient force. These forces can be calculated or summarized by the Maxwell stress tensor (MST) [25]. The optical forces exerted on particles are more intricate when plasmon enhancement is incorporated, as opposed to conventional optical tweezers. In this situation, the stress tensor around the target surface can be expressed as [26]:

$$T = \left[\epsilon_0 EE + \mu_0 HH - \frac{1}{2} (\epsilon_0 E^2 + \mu_0 H^2) I \right] \tag{8}$$

where E is the electric field intensity, H is the magnetic field intensity, ϵ_0 is the permittivity of the medium, μ_0 is the magnetic permeability of the medium, and I is the third-order unit tensor. The stress tensor is a symmetric tensor represented as follows [26]:

$$T = \begin{bmatrix} \epsilon_0 E_1^2 + \mu_0 H_1^2 - \frac{1}{2} (\epsilon_0 E^2 + \mu_0 H^2) & \epsilon_0 E_1 E_2 + \mu_0 H_1 H_2 & \epsilon_0 E_1 E_3 + \mu_0 H_1 H_3 \\ \epsilon_0 E_2 E_1 + \mu_0 H_2 H_1 & \epsilon_0 E_2^2 + \mu_0 H_2^2 - \frac{1}{2} (\epsilon_0 E^2 + \mu_0 H^2) & \epsilon_0 E_2 E_3 + \mu_0 H_2 H_3 \\ \epsilon_0 E_3 E_1 + \mu_0 H_3 H_1 & \epsilon_0 E_3 E_2 + \mu_0 H_3 H_2 & \epsilon_0 E_3^2 + \mu_0 H_3^2 - \frac{1}{2} (\epsilon_0 E^2 + \mu_0 H^2) \end{bmatrix} \tag{9}$$

Hence, the optical force exerted on particles in the electromagnetic field can be written as [27,28]:

$$F = \oint \langle T \rangle \cdot n dS \tag{10}$$

where n is the unit normal vector to the particle surface. When the optical force distribution of a particular particle is determined, the optical potential well depth at r_0 can be calculated by [29]:

$$U(r_0) = \int_\infty^{r_0} F(r) dr \tag{11}$$

The potential well depth used in the investigations characterizes the capture stability of particles. In order to suppress the Brownian motion of the nanoparticle, it is typically necessary for the depth of the potential well to satisfy the condition: $\exp(-U/k_B T) \ll 1$ [30].

2.3. Structure and Modeling

Figure 1a presents the schematic of the Si-nanostructured array consisting of four nanocuboids linearly arranged on the Si film. Each nanocuboid has a length of $l = 100$ nm,

width of $W = 40$ nm, and height of $h = 40$ nm, and the gap between two adjacent nanocuboids is $G = 20$ nm. The top view (X-Y) and front view (X-Z) of the nanoantenna are depicted in Figure 1b,c. The Si-nanostructured array coating on silicon film (SAS film) was designed by numerical simulations using the finite element method (FEM). With the development of microfabrication technologies, the SAS film can usually be fabricated by film deposition, photolithography, and ion-beam etching, among other techniques [31]. The plane wave is linearly polarized along the x-axis and propagates parallel to the negative direction of the y-axis. The SAS film is placed in water with a permittivity of 1.33. The refractive index of Si was extracted from Palik's handbook [32] and the target spherical nanoparticle was set as $n = 2$ with a diameter $D = 50$ nm.

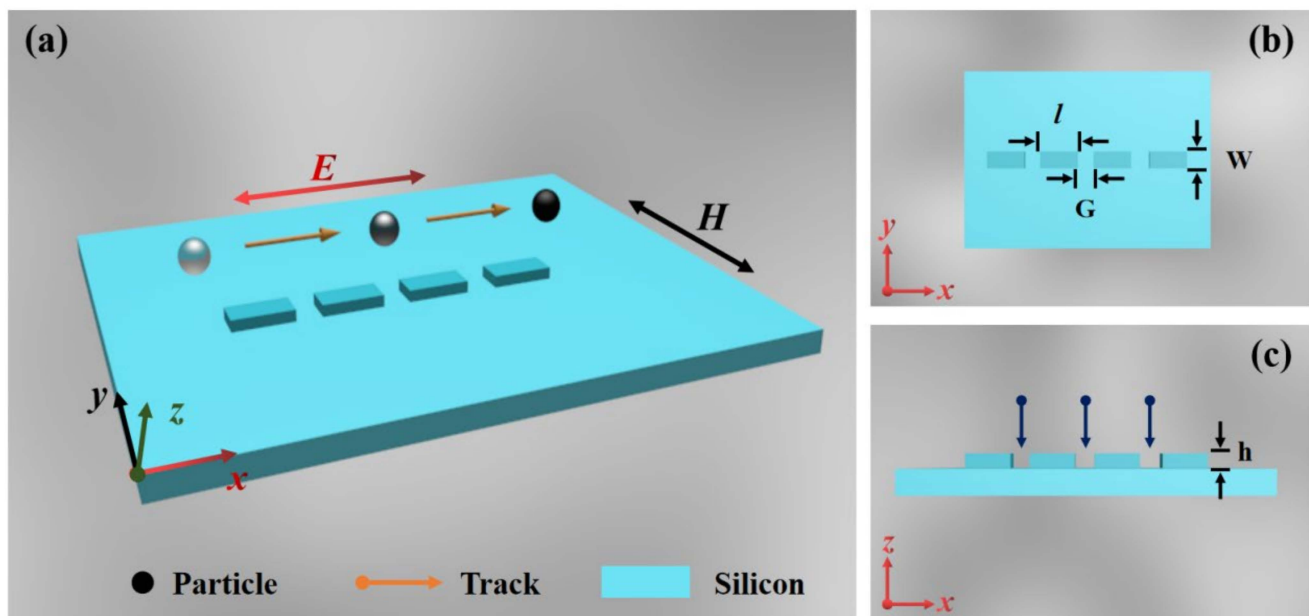


Figure 1. Schematic diagrams of the SAS film: (a) Three-dimensional (3D) view, (b) top view, and (c) front view.

The entire numerical simulation process was performed in COMSOL Multiphysics [33] (COMSOL, Inc., Burlington, MA, USA). The finite element method used in the simulations involves certain assumptions and simplifications to model the behavior of the SAS film accurately. The type and size of the mesh can affect the calculation results to different degrees. In addition, the type of coordinate system and the setting of boundary conditions for simulating the infinite space are also factors affecting the calculation results. With perfectly matched layer (PML) boundary conditions applied in all three dimensions to simulate a finite structure size, the spherical coordinate system is chosen as the simulation's reference coordinate system type. To reduce potential reflection, a scattering boundary condition (SBC) was applied to the outermost border. To capture the scattering energy, PML and SBC are used to end the simulation domain. SAS films use a finer mesh depending on the model's elemental order. The total number of elements in the mesh is 19,726, along with 3240 boundary and 424 edge elements, with a step of incidence wavelength of 21 from 750 nm to 2000 nm. In addition, the proposed SAS films can be completely fabricated by existing technology, which mainly consists of the following steps: cleaning the SOI substrate, using low-pressure chemical vapor deposition (LPCVD), spin-coating resist, utilizing electron beam lithography (EBL), developing and employing inductively coupled plasma (ICP) etching, and removing resist.

3. Results and Discussion

In order to explore the scattering features of the Si-nanostructured array coating on silicon film (SAS film), the scattering cross-section and electric field enhancement of the SAS

film were derived (Figure 2). As shown in Figure 2a, the SAS film shows significant scattering and extinction cross-sections, rendering it a promising candidate for surface-enhanced spectroscopies. The peaks of ECS and SCS are located at 1020 nm and 1480 nm and the SAS film has a negligible absorption cross-section in the near-infrared spectrum, resulting in ultra-low localized thermal energy generation during optical trapping. Consequently, the SAS film exhibits a broad spectrum of working wavelengths with negligible thermal effects. Figure 2b depicts the contributions of various multipoles to the scattering cross-section (SCS) in the wavelength range between 900 nm and 1800 nm. The SCS is dominated by the electric dipole moment (ED), whereas the other multipoles are negligible in comparison. The EQ, MD, and MQ contributions to the scattering cross-section is approximately zero and so the resonant peak at $\lambda = 1020$ nm in the total scattering spectrum is caused by the combination of ED and TD, while the resonant peak at 1480 nm in the total scattering response is attributed to the contributions of ED. The electric field enhancements for different incident light wavelengths are presented in Figure 2c. The electric field enhancement at point B is greater than those at points A, C, and D when the wavelength is shorter than 1100 nm. When the wavelength is longer than 1100 nm, the electric field enhancement at point B is comparatively lower than that at point A. Figure 2d–f displays the electric field enhancement for different wavelengths. The hotspot can be identified around the outer nanoparticles when the light wavelength is shorter than 1027 nm, while the enhancement of the local field around the inner nanoparticles is more obvious when $\lambda = 1240$ nm.

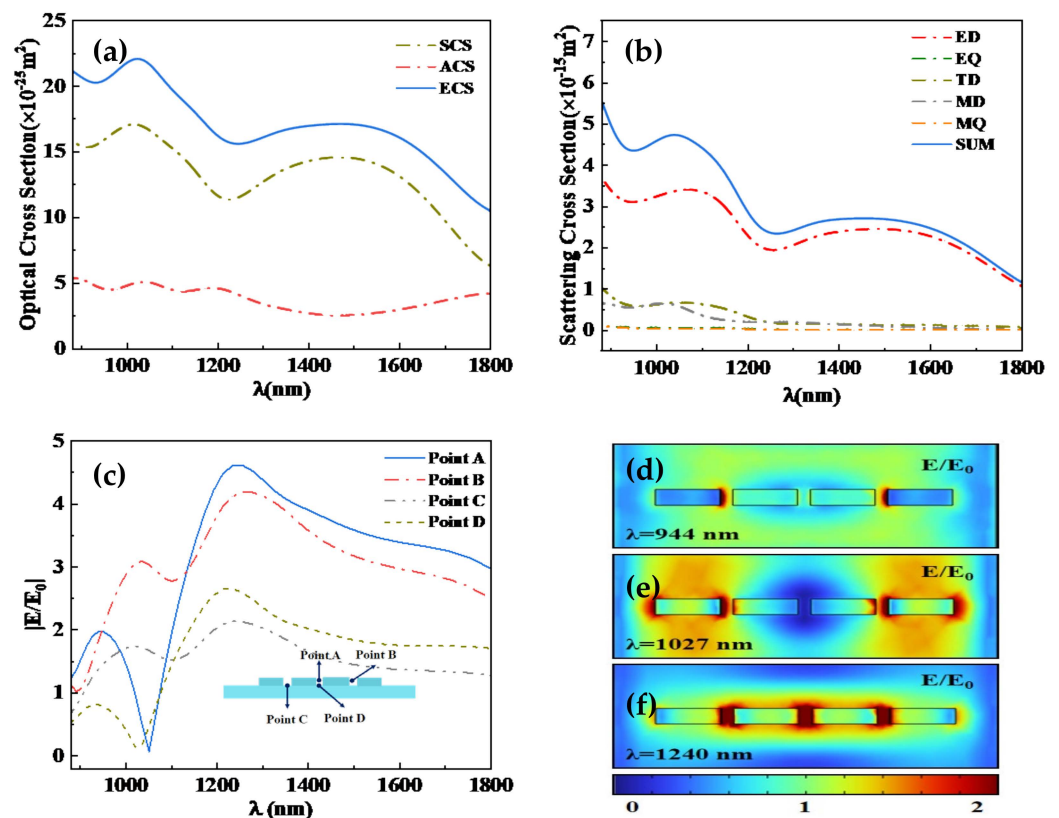


Figure 2. (a) Extinction, absorption, and scattering cross-sections of the Si-nanostructured array coating on silicon film (SAS film), (b) contributions of different multipoles to the scattering cross-sections, (c) electric field enhancement for different incident wavelengths. Electric field distributions: (d) $\lambda = 944$ nm, (e) $\lambda = 1027$ nm, and (f) $\lambda = 1240$ nm.

Structural parameters as well as surface topography play a crucial role in the electric field strength, which in turn leads to differences in the ability to capture nanoparticles [33,34]. The parameters are optimized by examining the electric field enhancement at different incident wavelengths, as shown in Figure 3. Two different plasmon resonance peaks appear

from the electric field enhancement curve at 944 nm and 1240 nm for points A and D, while two peaks at 1027 nm and 1240 nm are observed from points B and C. As shown in Figure 3, the field enhancement exhibits an upward trend as the gap distance decreases from 20 nm to 80 nm. Based on this observation, the gap distance was set as 20 nm in the subsequent study. The field enhancement can be improved by operating at a longer wavelength up to 1240 nm, but the enhancement diminishes at wavelengths longer than 1240 nm. Accordingly, taking into account the popular 1064 nm infrared laser, the wavelengths of the incident light are set at 1064 nm and 1240 nm.

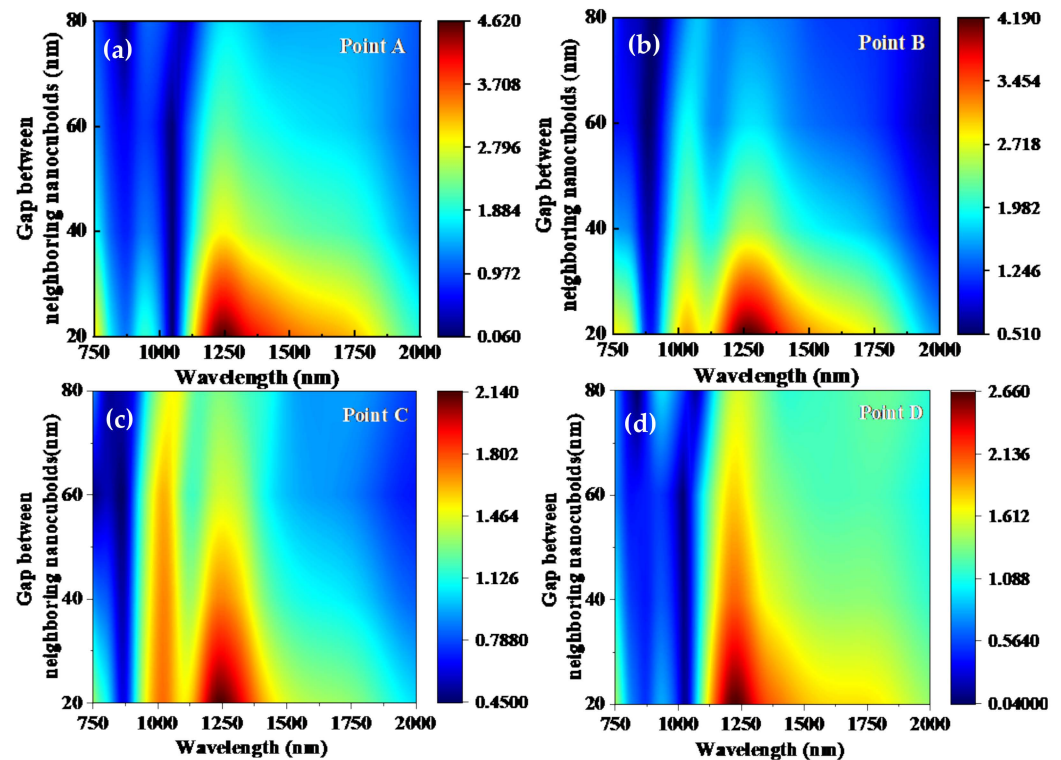


Figure 3. Field enhancement for different gap distances and wavelengths: (a) Point A, (b) point B, (c) point C, and (d) point D.

The optical forces generated by the Si-nanostructured array coating on silicon film (SAS film) as a nanotweezer were determined for the optical trapping of a nanosphere for $\lambda = 1064$ nm. Numerical analysis was performed to determine the relationship between the center position of the nanoparticle (x_c, y_c, z_c) and the optical forces (F_x, F_y, F_z), where F_x, F_y , and F_z represent the x, y , and z components of the optical force vector, respectively. The optical force distribution surrounding the SAS film is acquired by moving the nanosphere along the x and y axes. By determining the optical forces F_x and F_z as well as the potential well shown in Figure 4a,c, there exist a total of four stable capture points along the x -axis. The stable trapping equilibrium point (zero force in a certain direction) is found at $x_c = -235$ nm, -119 nm, 119 nm, and 235 nm, respectively. As shown in Figure 4b, the y -component of the force for $x = 120$ nm and $x = 240$ nm consistently exhibits a negative value, implying an attractive interaction with the nanosphere situated above it. In addition, F_y is negative for $y_c < 0$ and positive for $y_c > 0$ because the Brownian motion causes the nanosphere to deviate from the equilibrium point [35]. These results suggest that the gaps of the SAS film result in forces to enable optical trapping of nanoparticles along the x -, y -, and z -axis.

A comparative analysis was conducted to determine the optical forces and potential well distributions for $\lambda = 1200$ nm and 1240 nm. As shown in Figure 5, F_x rises gradually to a maximum as the nanosphere moves along the x -axis, and then decreases to zero at $x = 0$ nm. The potential U_x exhibits a valley-like energy profile, indicating trapping at $x_c = 0$ nm, as

shown in Figure 5a,b. However, the optical force F_z in Figure 5c,d indicates small repulsion between the nanoparticles located in the central region of the Si-nanostructured array coating on silicon film (SAS film). In contrast to results observed at 1064 nm, there is no stable capturing point for $\lambda = 1200$ nm and $\lambda = 1240$ nm.

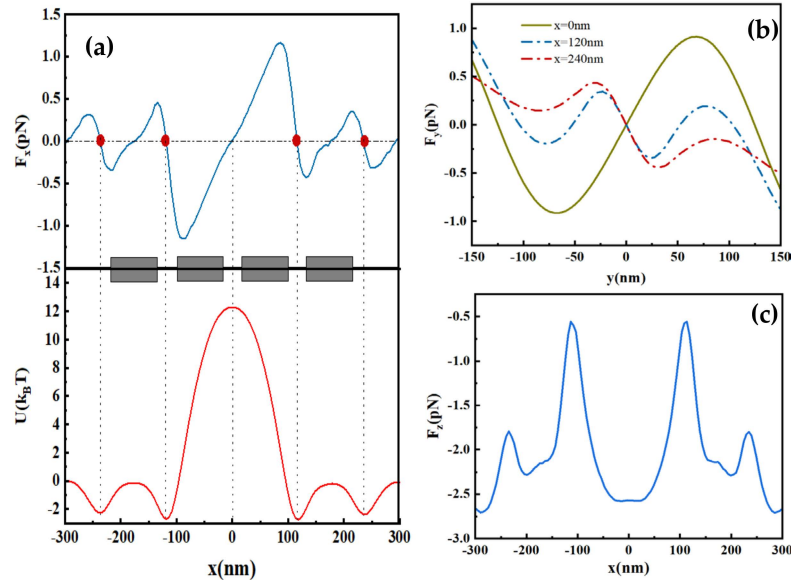


Figure 4. MST optical forces and trapping potentials for a nanosphere for $\lambda = 1064$ nm: (a) Optical forces F_x and potential well U vs. NS center position along the x -axis, (b) optical forces F_y vs. NS center position along the y -axis, and (c) optical forces F_z vs. NS center position along the x -axis.

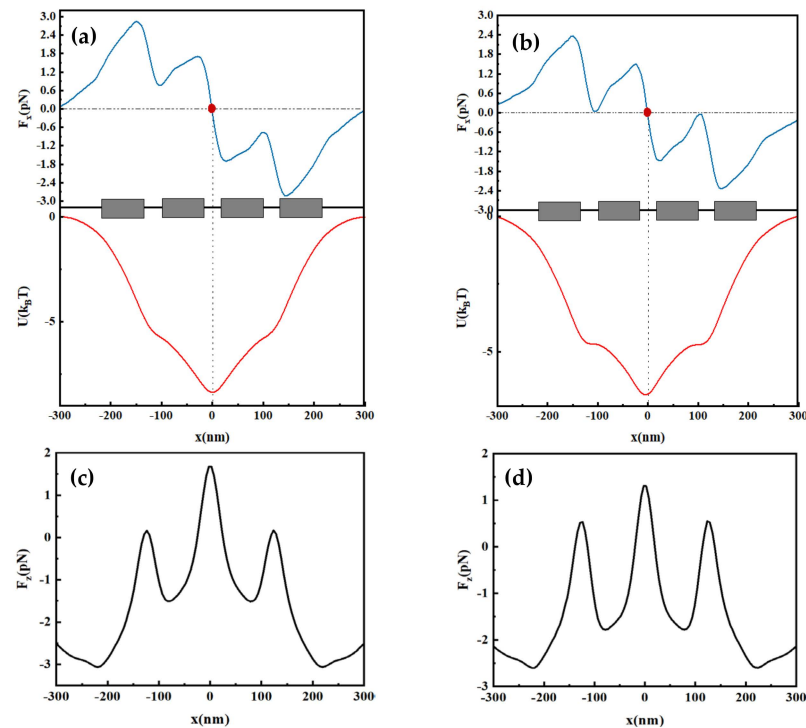


Figure 5. MST optical forces and trapping potentials for a nanosphere: (a,c) $\lambda = 1240$ nm and (b,d) 1200 nm.

In order to discuss the upper limits of nanoparticle sizes that the SAS film can effectively trap and manipulate, Figure 6 depicts the optical forces and trapping potentials in the x -direction for different nanosphere radius. It can be seen from Figure 6a that the

optical force F_x exerted on the nanosphere exhibits a significant variation as the radius of the nanosphere increases. There exist four stable capture points in the x -direction when the radius (r) is equal to 25 nm, while the number of stable capture points decreases to zero when the radius is increased to 50 nm. Figure 6b illustrates the presence of multiple energy wells as the radius increases to 45 nm around the SAS film in the gap, which implies that it should be possible to trap multiple nanoparticles. Hence, nanoparticle sizes with an upper limit of $r = 45$ nm are able to be effectively trapped and manipulated within the SAS film.

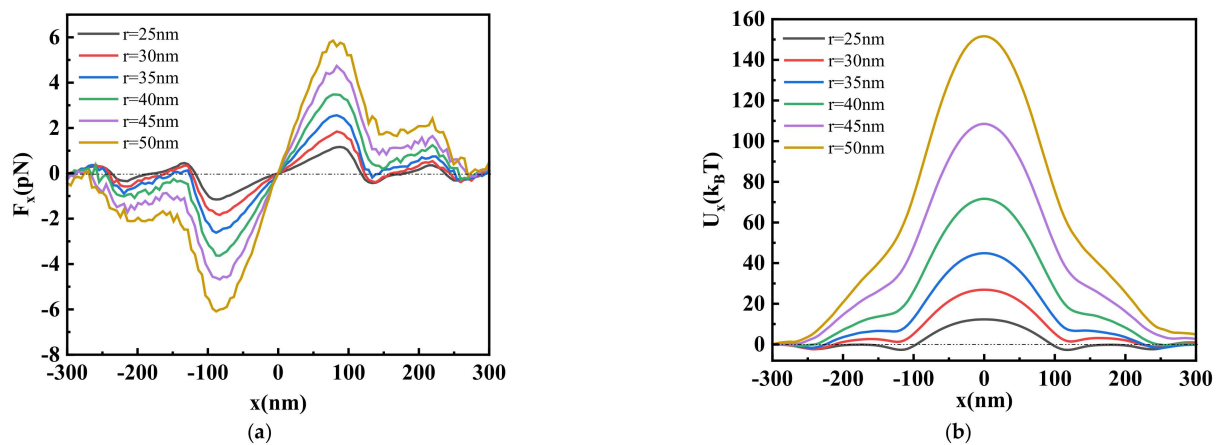


Figure 6. (a) Optical forces and (b) trapping potentials in the x -direction for different nanosphere radius (r).

The optical force F_z acting on the nanosphere and Si-nanostructured array coating on silicon film (SAS film) was evaluated for different parameters. Figure 7a–d shows the optimization process for the four different parameters of array height (h), nanosphere refractive index (n), array width (W), and nanosphere radius (r). As shown in Figure 7a,b, the optical force F_z decreases gradually with increasing array height (h) and width (W). Moreover, F_z shows minimal repulsion between nanospheres on both sides of the central region for $h = 45$ nm and $W = 60$ nm. The z -component of the optical force exerted on the nanoparticles with different refractive index (n) and radius (r) is determined when the nanoparticles are 10 nm above the SAS film. According to Figure 7c,d, the optical force acting on the nanosphere shows subtle change with increasing refractive index (n), while the optical force F_z increases gradually with the nanosphere radius (r).

To investigate the impact of the thermophoresis force on particle capture, numerical analysis was conducted regarding the increase in the temperature in the proximity of the Si-nanostructured array coating on silicon film (SAS film), as shown in Figure 8. The thermal conductivity in the simulation was set to be $K_{Si} = 148 \text{ WK}^{-1}\text{m}^{-1}$ for Si. Figure 8a shows the power dissipation density of the SAS film, and a majority of the power dissipation is close to the surface of the SAS film. The steady-state temperature profile of the SAS film in Figure 8b indicates a peak of approximately 0.02 K. As a result, the relatively low steady-state temperature gives rise to minimal thermal energy generation during optical trapping.

The optical force distributions of the particles for different refractive indexes are displayed in Figure 9. The optical force F_y is determined by analyzing the variations at the equilibrium points as a function of the refractive index of the nanosphere between 1.5 and 2 in the trapping region. As shown in Figure 9a, the structure comprises three rows of nanoarrays, each with gradually increasing gap distances of $G = 20$ nm, $G = 30$ nm, and $G = 40$ nm, respectively. The incident wavelength is 1064 nm. The distribution of the optical force around the Si-nanostructured multiple array coatings on silicon film is obtained by manipulating the position of the nanosphere along the y -axis. As displayed in Figure 9b, the nanosphere can be captured at distinct gaps when subjected to different forces. In cases where the captured nanosphere experiences a deviation from the gap center

in the x-direction, it will be subjected to the optical force and ultimately return to the gap center. The optical force exerted on the nanosphere also increases with increasing refractive index. Moreover, the optical force experienced by the particles for a specific refractive index increases through the three rows of nanoarrays. The results indicate the function of an optical tweezer for particle sorting.

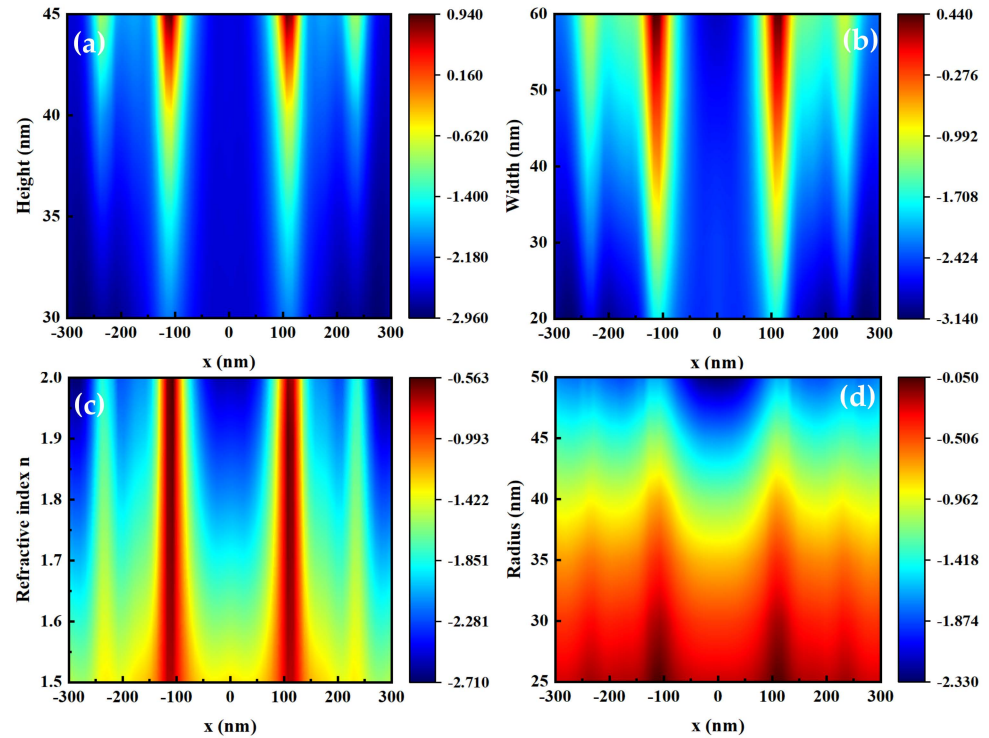


Figure 7. Optical forces in the z-direction for (a) array height (h), (b) nanosphere refractive index (n), (c) array width (W), and (d) nanosphere radius (r).

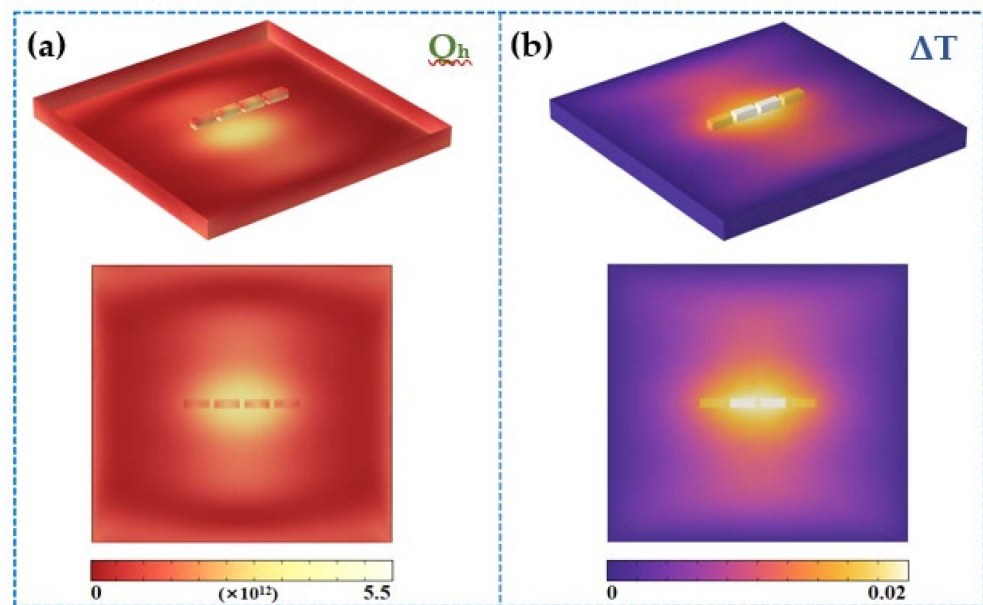


Figure 8. (a) Heat power dissipation density around the Si-nanostructured array coating on silicon film (SAS film) and (b) temperature profile around the SAS film.

The Si-nanostructured array coating on silicon film (SAS film) is irradiated with left circularly polarized (LCP) light, right circularly polarized (RCP) light, and a Gaussian beam

as shown Figure 10a. Figure 10b shows the schematic in which the nanosphere illuminated by the Gaussian beam propagates along the z-axis with polarization along the x-axis for a beam width of 1200 nm. The optical force exerted on a trapped nanoparticle is shown in Figure 10c–e. Upon irradiation by the circularly polarized light and Gaussian beam, two stable capturing points appear along the x-axis, and the nanosphere is able to move freely between gaps in the nanoarray due to the loose potential well. Compared with circularly polarized illumination and the Gaussian beam, the optical trapping features of a nanosphere are superior during linearly polarized light exposure. The use of circularly polarized illumination and the Gaussian beam augments the trapping region and probability of a moving nanoparticle to be pulled into the SAS film, which is suitable for applications in optical tweezers and plasma coatings.

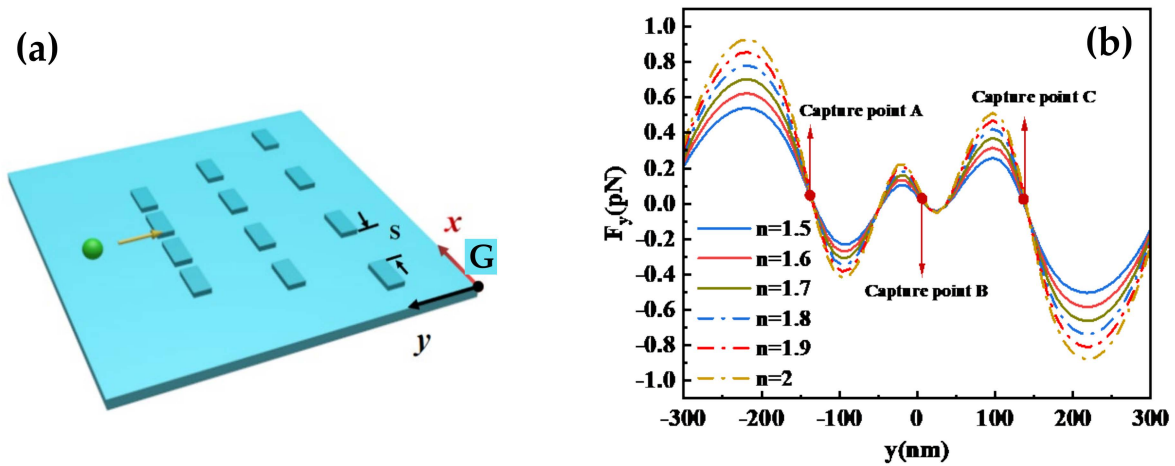


Figure 9. (a) Schematic diagram of the Si-nanostructured multiple array coatings on silicon film and (b) optical force distributions of the particles with different refractive indexes.

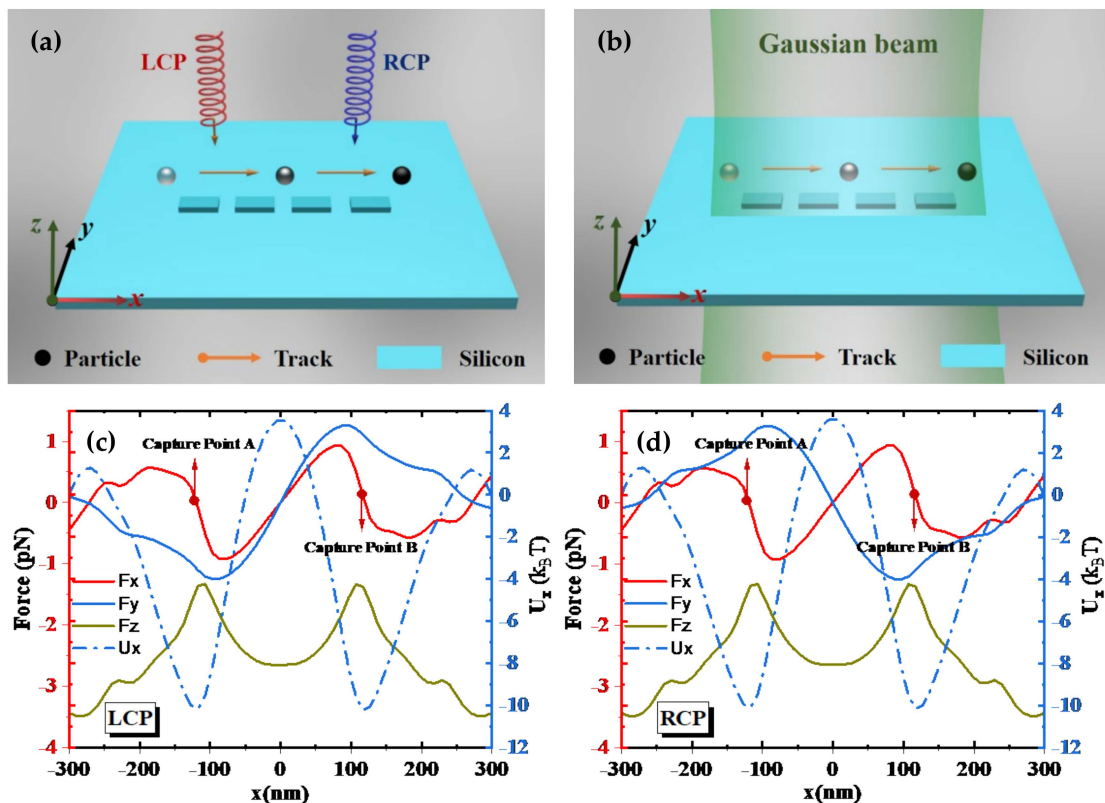


Figure 10. Cont.

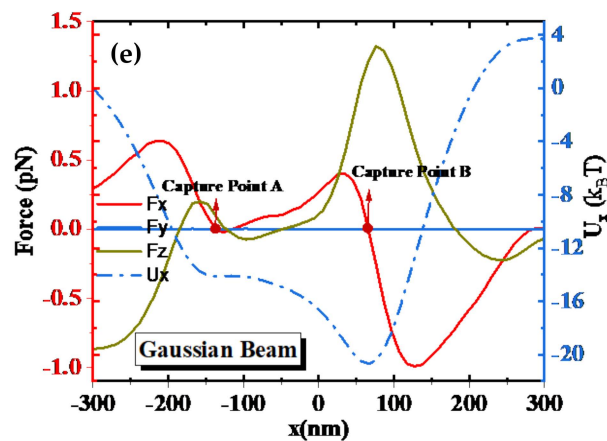


Figure 10. Schematic diagram of the Si-nanostructured array coating on silicon film: (a) Circularly polarized illumination, (b) Gaussian beam, and (c–e) optical force distributions of the particles under different polarization conditions.

A comparative analysis of representative optical trapping techniques or materials is presented in Table 1 and our structure indeed delivers excellent performance.

Table 1. Comparison of the properties of optical trapping structures.

References	Characteristics	Wavelength Range (nm)	Optical Force	Structure Diagram
[35]	Si nanotrimer on a Si substrate Particle r = 10–15 nm	600–1200	One capture point	
[36]	Si nanonamer on a glass substrate Nanowire r = 15 nm	1064	Trapping of multiple nanowires	
[37]	Coupled T-shaped Cu nanoantenna on a glass substrate Particle r = 15 nm	1064	One capture point	
[38]	Au bowtie aperture and Au thin film on a glass substrate Particle r = 50 nm	1100–1200	One capture point	

Table 1. Cont.

References	Characteristics	Wavelength Range (nm)	Optical Force	Structure Diagram
[7]	Coaxial plasmonic aperture (a dielectric ring embedded in a noble metal) Particle $r = 5$ nm	400–800	Two capture point	
[39]	Gold bowtie structure and ITO film on a glass substrate Particle $r = 2$ nm	532	Two capture point	
This work	Si-nanostructured array coating on silicon film (SAS film) Particle $r = 25$ –45 nm	900–1800	Four capture point	

4. Conclusions

A silicon-nanostructured array coating on silicon film (SAS film) was designed and demonstrated for the optical trapping of single dielectric nanoparticles and the related plasmonic and optical properties were determined. The SAS film shows stable optical trapping of nanoparticles as small as 25 nm, and the four energy wells around the nanoarray enable capturing of multiple nanoparticles at a wavelength of 1064 nm. The electric field enhancement increases with decreasing gap distance and the optical force exhibits a correlation with the structural parameters of the silicon nanoarray, as well the refractive index and radius of the captured nanoparticles. When the nanoarray is excited by circularly polarized light and the Gaussian beam, two optical traps are observed, indicating the possibility of trapping nanoparticles. The Si-nanostructured array coating on silicon film exhibits excellent enhancement of the near-field electric field and optical trapping characteristics, and our results provide theoretical guidance for the research and development of lab-on-a-chip devices and optical information processing.

Author Contributions: Conceptualization, W.Z. and D.W.; methodology, Y.R.; software, W.Z.; validation, J.L.; formal analysis, W.Z.; investigation, D.W.; resources, Y.Y.; data curation, W.L.; writing—original draft preparation, W.Z.; writing—review and editing, C.L. and P.K.C.; visualization, X.X.; supervision, C.L.; project administration, W.Z. and C.L.; funding acquisition, J.L. and P.K.C. All authors have read and agreed to the published version of the manuscript.

Funding: This research was funded by the Outstanding Young and Middle-Aged Research and Innovation Team of Northeast Petroleum University (No. KYCXTD201801), the Heilongjiang Provincial Natural Science Foundation of China (No. JQ2023F001), the China Postdoctoral Science Foundation (No. 2020M670881), the Study Abroad returnees merit-based Aid Foundation in Heilongjiang Province (No. 070-719900103), Northeast Petroleum University scientific research projects (No. 2019KQ74), City University of Hong Kong Donation Research Grants (No. DON-RMG 9229021 and 9220061), and the Strategic Research Fund of the City University of Hong Kong (SRG) (No. 7005505).

Institutional Review Board Statement: Not applicable.

Informed Consent Statement: Not applicable.

Data Availability Statement: Not applicable.

Conflicts of Interest: The authors declare no conflict of interest.

References

1. Ashkin, A. Acceleration and trapping of particles by radiation pressure. *Phys. Rev. Lett.* **1970**, *24*, 156–159. [[CrossRef](#)]
2. Perkins, T.T.; Quake, S.R.; Smith, D.; Chu, S. Surface vibrational spectroscopic studies of hydrogen bonding and hydrophobicity. *Science* **1994**, *264*, 826–828.
3. Pralle, A.; Florin, E.; Stelzer, E.H.K.; Horber, J.K.H. Local viscosity probed by photonic force microscopy. *Appl. Phys. A* **1998**, *66*, S71–S73. [[CrossRef](#)]
4. Greenleaf, W.J.; Woodside, M.T.; Abbondanzieri, E.A.; Block, S.M. Passive all-optical force clamp for high-resolution laser trapping. *Phys. Rev. Lett.* **2005**, *95*, 208102. [[CrossRef](#)]
5. Grier, D.G. A revolution in optical manipulation. *Nature* **2003**, *424*, 810–816. [[CrossRef](#)]
6. Li, H.; Ren, Y.; Li, Y.; He, M.; Gao, B.; Qi, H. Nanoparticle manipulation using plasmonic optical tweezers based on particle sizes and refractive indices. *Opt. Express* **2022**, *30*, 34092. [[CrossRef](#)]
7. SamadiSamadi, M.; Alibeigloo, P.; Aqhili, A.; Khosravi, M.A.; Saeidi, F.; Vasini, S.; Ghorbanzadeh, M.; Darbar, S.; Moravvej-Farshi, M.K. Plasmonic tweezers: Towards nanoscale manipulation. *Opt. Lasers Eng.* **2022**, *154*, 107001. [[CrossRef](#)]
8. Schuller, J.A.; Barnard, E.S.; Cai, W.; Jun, Y.C.; White, J.S.; Brongersma, M.L. Plasmonics for extreme light concentration and manipulation. *Nat. Mater.* **2010**, *9*, 193–204. [[CrossRef](#)] [[PubMed](#)]
9. Barnes, W.L.; Dereux, A.T.; Ebbesen, W. Surface plasmon subwavelength optics. *Nature* **2003**, *424*, 824–830. [[CrossRef](#)] [[PubMed](#)]
10. Yoo, D.; Gurunatha, K.L.; Choi, H.-K.; Mohr, D.A.; Ertsgaard, C.T.; Gordon, R.; Oh, S.-H. Low-Power Optical Trapping of Nanoparticles and Proteins with Resonant Coaxial Nanoaperture Using 10 nm Gap. *Nano Lett.* **2018**, *18*, 3637–3642. [[CrossRef](#)] [[PubMed](#)]
11. Satter, S.S.; Mahdy, M.R.C.; Ohi, M.A.R.; Islam, F.; Rivy, H.M. Plasmonic cube tetramers over substrates: Reversal of binding force as the effect of fano resonance and light polarization. *J. Phys. Chem. C* **2018**, *122*, 20923–20934. [[CrossRef](#)]
12. Zhang, Q.; Xiao, J.J. Multiple reversals of optical binding force in plasmonic disk-ring nanostructures with dipole-multipole Fano resonances. *Opt. Lett.* **2013**, *38*, 4240–4243. [[CrossRef](#)]
13. Pang, Y.; Gordon, R. Optical trapping of a single protein. *Nano Lett.* **2011**, *12*, 402. [[CrossRef](#)] [[PubMed](#)]
14. Gao, D.; Shi, R.; Huang, Y.; Gao, L. Fano-enhanced pulling and pushing optical force on active plasmonic nanoparticles. *Phys. Rev. A* **2017**, *96*, 043826. [[CrossRef](#)]
15. Jiang, M.; Wang, G.; Xu, W.; Ji, W.; Zou, N.; Ho, H.-P.; Zhang, X. Two-dimensional arbitrary nano-manipulation on a plasmonic metasurface. *Opt. Lett.* **2018**, *43*, 1602–1605. [[CrossRef](#)]
16. Khurgin, J.B.; Jacob, B. How to deal with the loss in plasmonics and metamaterials. *Nat. Nanotechnol.* **2015**, *10*, 2–6. [[CrossRef](#)] [[PubMed](#)]
17. Xu, Z.; Song, W.; Crozier, K.B. Optical Trapping of Nanoparticles Using All-Silicon Nanoantennas. *ACS Photon.* **2018**, *5*, 4993–5001. [[CrossRef](#)]
18. Yang, Y.; Ren, Y.X.; Chen, M.; Arita, Y.; Rosales-Guzmán, C. Optical trapping with structured light: A review. *Adv. Photonics* **2021**, *3*, 034001. [[CrossRef](#)]
19. Xu, Z.; Crozier, K.B. All-dielectric nanotweezers for trapping and observation of a single quantum dot. *Opt. Express* **2019**, *27*, 4034. [[CrossRef](#)] [[PubMed](#)]
20. Shi, Y.; Song, Q.; Toftul, I.; Zhu, T.; Yu, Y.; Zhu, W.; Tsai, D.P.; Kivshar, Y.; Liu, A.Q. Optical manipulation with metamaterial structures. *Appl. Phys. Rev.* **2022**, *9*, 031303. [[CrossRef](#)]
21. Liu, L.; Ge, L. Toroidal dipole resonances by a sub-wavelength all-dielectric torus. *Opt. Express* **2022**, *30*, 7491–7500. [[CrossRef](#)] [[PubMed](#)]
22. Savinov, V.; Fedotov, V.A.; Zheludev, N.I. Toroidal dipolar excitation and macroscopic electromagnetic properties of metamaterials. *Phys. Rev. B* **2014**, *89*, 205112. [[CrossRef](#)]
23. Zhang, X.; Zhang, Q.; Yuan, Y.; Liu, J.; Liu, X. Ultra-directional forward scattering by a high refractive index dielectric T-shaped nanoantenna in the visible. *Phys. Letter. A* **2020**, *384*, 126696. [[CrossRef](#)]
24. Xu, C.; Cheng, K.; Li, Q.; Shang, X.; Wu, C.; Wei, Z.; Zhang, X.; Li, H. The dual-frequency zero-backward scattering realized in a hybrid metallo-dielectric nanoantenna. *AIP Adv.* **2019**, *9*, 075121. [[CrossRef](#)]
25. Rohrbach, A.; Stelzer, E.H. Optical Trapping of Dielectric Particles in Arbitrary Fields. *J. Opt. Soc. Am. A* **2001**, *18*, 839–853. [[CrossRef](#)]
26. Yang, X.; Liu, Y.; Oulton, R.F.; Yin, X.; Zhang, X. Optical Forces in Hybrid Plasmonic Waveguides. *Nano Lett.* **2011**, *11*, 321–328. [[CrossRef](#)]
27. Wan, T.; Tang, B. Efficient Prediction and Analysis of Optical Trapping at Nanoscale via Finite Element Tearing and Interconnecting Method. *Nanoscale Res. Lett.* **2019**, *14*, 294. [[CrossRef](#)]
28. Ghorbanzadeh, M.; Darbari, S.; Moravvej-Farshi, M.K. Graphene-Based Plasmonic Force Switch. *Appl. Phys. Lett.* **2016**, *108*, 111105. [[CrossRef](#)]

29. Novotny, L.; Bian, R.X.; Xie, X.S. Theory of Nanometric Optical Tweezers. *Phys. Rev. Lett.* **1997**, *79*, 645. [[CrossRef](#)]
30. Ashkin, A.; Dziedzic, J.M.; Bjorkholm, J.E.; Chu, S. Observation of a Single-Beam Gradient Force Optical Trap for Dielectric Particles. *Opt. Lett.* **1986**, *11*, 288–290. [[CrossRef](#)] [[PubMed](#)]
31. Xiong, Y.; Liu, X.; Zhang, J.; Wang, X.; Wang, X.; Gao, J.; Yang, H. High-Performance Ultra-Broadband for Polarized Long-Wavelength Infrared Light Trapping. *Coatings* **2022**, *12*, 1194. [[CrossRef](#)]
32. Palik, E.D. *Handbook of Optical Constants of Solids*; Academic Press: New York, NY, USA, 1985.
33. Zhu, J.; Hu, D.; Wang, Y.; Tao, C.; Jia, H.; Zhao, W. Efficient Light Trapping from Nanorod-Like Single-Textured Al-Doped ZnO Transparent Conducting Films. *Coatings* **2021**, *11*, 513. [[CrossRef](#)]
34. Wang, S.; Liu, H.; Ma, K.; Ou, Q.; Geng, H.; Lv, F. Effect of Particle Trap on Motion Characteristics of Metal Particles in AC GILs and Parameter Optimization. *Coatings* **2022**, *12*, 981. [[CrossRef](#)]
35. Guo, Y.; Liao, Y.; Yu, Y.; Shi, Y.; Xiong, S. Nanoparticle trapping and manipulation using a silicon nanotrimer with polarized light. *Opt. Lett.* **2020**, *45*, 5604–5607. [[CrossRef](#)] [[PubMed](#)]
36. Li, R.; Zhao, Y.; Ge, Y.; Xu, Z. Optical trapping and manipulation of nanowires using multi-hotspot dielectric nanonamers. *AIP Adv.* **2022**, *12*, 065128. [[CrossRef](#)]
37. Li, R.; Zhao, Y.; Li, R.; Liu, H.; Ge, Y.; Xu, Z. Plasmonic optical trapping of nanoparticles using T-shaped copper nanoantennas. *Opt. Express* **2021**, *29*, 9826–9835. [[CrossRef](#)]
38. Lin, Y.; Lee, P. Efficient Optical Trapping and Detection of Nanoparticle Via Plasmonic Bowtie Notch. *IEEE Photonics J.* **2019**, *11*, 4800610. [[CrossRef](#)]
39. Zhang, W.; Zhang, Y.; Zhang, S.; Wang, Y.; Yang, W.; Min, C.; Yuan, X. Nonlinear modulation on optical trapping in a plasmonic bowtie structure. *Opt. Express* **2021**, *29*, 11664–11673. [[CrossRef](#)]

Disclaimer/Publisher’s Note: The statements, opinions and data contained in all publications are solely those of the individual author(s) and contributor(s) and not of MDPI and/or the editor(s). MDPI and/or the editor(s) disclaim responsibility for any injury to people or property resulting from any ideas, methods, instructions or products referred to in the content.